EES Solar

PAPER

View Article Online
View Journal | View Issue

Cite this: *EES Sol.*, 2026, **2**, 436

How nanotextured interfaces influence the electronics in perovskite solar cells

Dilara Abdel, [a] Jacob Relle, [bc] Thomas Kirchartz, [de] Patrick Jaap, [f] Jürgen Fuhrmann, [f] Sven Burger, [cg] Christiane Becker, *[bh] Klaus Jäger *[bc] and Patricio Farrell *[a]

Perovskite solar cells have reached power conversion efficiencies that rival those of established silicon photovoltaics. Nanotextures in perovskite solar cells scatter the incident light, thereby improving optical absorption. In addition, experiments show that nanotextures impact electronic performance, although the underlying mechanisms remain unclear. This study investigates the underlying theoretical reasons by combining multi-dimensional optical and charge-transport simulations for a single-junction perovskite solar cell. Our numerical results reveal that texturing redistributes the electric field, influencing carrier accumulation and recombination dynamics. We find that moderate texturing heights (≤300 nm) always increase the power conversion efficiency, regardless of surface recombination velocities. Our study also clarifies why experiments have reported that texturing both increased and reduced open-circuit voltages in perovskite solar cells: this behaviour originates from variations in surface recombination at the untextured electron transport layer. In contrast, surface recombination at the textured hole transport layer strongly affects the short-circuit current density, with lower recombination rates keeping it closer to the optical ideal. These findings provide new insights into the opto-electronic advantages of texturing and offer guidance for the design of next-generation textured perovskite-based solar cells, light emitting diodes, and photodetectors.

Received 12th December 2025
Accepted 28th December 2025

DOI: 10.1039/d5el00208g

rsc.li/EESSolar

Broader context

Perovskite solar cells have experienced astonishing improvements in recent years, and their power conversion efficiencies have caught up with that of market-dominating silicon solar cells. Time and again, perovskites have surprised us with excellent opto-electronic material properties. In this article, we address two seemingly contradictory experimental observations: nanotextured perovskite solar cells have been reported to exhibit both higher and lower open-circuit voltages compared to planar devices. To resolve this discrepancy, we investigate how nanotexturing influences the optoelectronic device performance by combining accurate optical and electrical simulations based on the finite element and finite volume methods, respectively. For non-conformal layer textures, our simulations reveal that the diverging voltage behaviours can be traced back to variations in the passivation quality of the transport layers, which can either reduce or enhance recombination losses. By shedding light on this mechanism, our work deepens the understanding of perovskite-based photovoltaics and shows ways to further improve the design and efficiency of this technology.

Introduction

In recent years, perovskite-based solar cells have rapidly advanced photovoltaics by combining high power conversion efficiencies (PCEs) with low-cost and scalable fabrication methods. Their outstanding opto-electronic properties, such as tunable band gaps or strong absorption, make them highly attractive for next-generation solar energy applications.[1,2]

Multi-junction solar cells, comprising multiple sub-cells with different bandgaps, mitigate thermalisation losses and thereby enhance the PCE (see, *e.g.*, ref. 3, chapter 7). In tandem solar cells two junctions are combined. Both all-perovskite and perovskite-silicon tandem devices have surpassed the efficiency limit of traditional single-junction silicon cells.[4–8] These improvements are driven by advances in material composition, interface passivation, and increasingly sophisticated device architectures.

[a]*Numerical Methods for Innovative Semiconductor Devices, Weierstrass Institute for Applied Analysis and Stochastics (WIAS), Berlin, Germany. E-mail: patricio.farrell@wias-berlin.de*

[b]*Dept. Optics for Solar Energy, Helmholtz-Zentrum Berlin für Materialien und Energie GmbH, Berlin, Germany. E-mail: christiane.becker@helmholtz-berlin.de; klaus.jaeger@helmholtz-berlin.de*

[c]*Computational Nano Optics, Zuse Institute Berlin, Berlin, Germany*

[d]*IMD-3 Photovoltaics, Forschungszentrum Jülich GmbH, Jülich, Germany*

[e]*Faculty of Engineering and CENIDE, University of Duisburg-Essen, Duisburg, Germany*

[f]*Numerical Mathematics and Scientific Computing, Weierstrass Institute for Applied Analysis and Stochastics (WIAS), Berlin, Germany*

[g]*JCMwave GmbH, Berlin, Germany*

[h]*Hochschule für Technik und Wirtschaft Berlin, Berlin, Germany*

Introducing textured interfaces is a commonly used strategy to further enhance device performance. In most studies on perovskite solar cells, texturing has been mainly motivated and discussed from an optical perspective.[9–13] Pioneering studies have demonstrated enhanced light absorption and short-circuit current densities J_{SC} in perovskite-silicon tandem devices, featuring pyramidal textures on the micrometer and sub-micrometer scale.[10–12] However, the texture-related increase of J_{SC} was often accompanied by a reduced electronic performance in terms of open-circuit voltage V_{OC}.[9,14]

Beyond these optically motivated and experimentally verified enhancements in short-circuit current density J_{SC}, several experimental studies have also reported *increases* of the open-circuit voltage V_{OC} in textured perovskite solar cells. In single-junction devices, for instance, V_{OC} gains of up to +20 mV have been measured, which cannot be explained by the weak logarithmic dependence of V_{OC} on J_{SC}.[13,19] Similarly, beneficial but unexplained voltage gains between +15 mV and +45 mV have been reported in tandem architectures.[12,20,21] Proposed mechanisms include improved charge carrier collection due to a widened depletion region[12] and suppressed non-radiative recombination.[22] However, a detailed physical understanding of the enhancement or reduction of V_{OC} in textured devices is still lacking. As interfaces are known to play a crucial role on non-radiative recombination and voltage losses in perovskite solar cells,[23] surface-enlarging textures will have a significant impact on the V_{OC} of the devices.

Opto-electronic simulations can help to study perovskite solar cells, including vacancy migration and advanced light absorption models. Often, commercial software tools are used,[24–26] which typically lack the flexibility to implement customised physical models. As an alternative, (partially) open-source simulation tools have been developed to study vacancy-assisted charge transport.[27–30] However, such one-dimensional approaches are inherently limited in their ability to capture the spatial effects introduced by nanoscale textures. Recent multi-dimensional studies have begun to simulate textured perovskite architectures, particularly in tandem devices. Still, these works primarily focus on device optimization, without offering insight into underlying physics.[22,31,32]

In this work, we present a multi-dimensional simulation framework, applied here in two spatial dimensions, which couples optical finite element simulations of the time-harmonic Maxwell equations *via* `JCMsuite`[33] with electronic finite volume simulations using `ChargeTransport.jl`,[34,35] which solve the drift-diffusion equations. The optical simulations allow us to generate geometry-dependent photogeneration profiles, which are passed to the electronic solver that calculates coupled electronic–ionic charge carrier transport in the textured perovskite solar cell. This integrated approach allows us to quantify how nanotextures influence carrier dynamics.

The remainder of this paper is structured as follows: we first present a well-studied planar single-junction perovskite solar cell architecture from the literature,[16–18] which serves as the baseline for this study. Then, we describe the extensions introduced to model the textured cells. Finally, we analyse the influence of texture height on light absorption and key performance indicators, including short-circuit current density, open-circuit voltage, and power conversion efficiency. To uncover the mechanism behind the enhanced efficiencies, we identify the dominant recombination mechanism, and demonstrate that a redistribution of the electric field governs the electronic response.

Results and discussion

Perovskite solar cell simulation setup

The motivation for this study are two seemingly contradictory experimental findings: nanotextured perovskite solar cells have

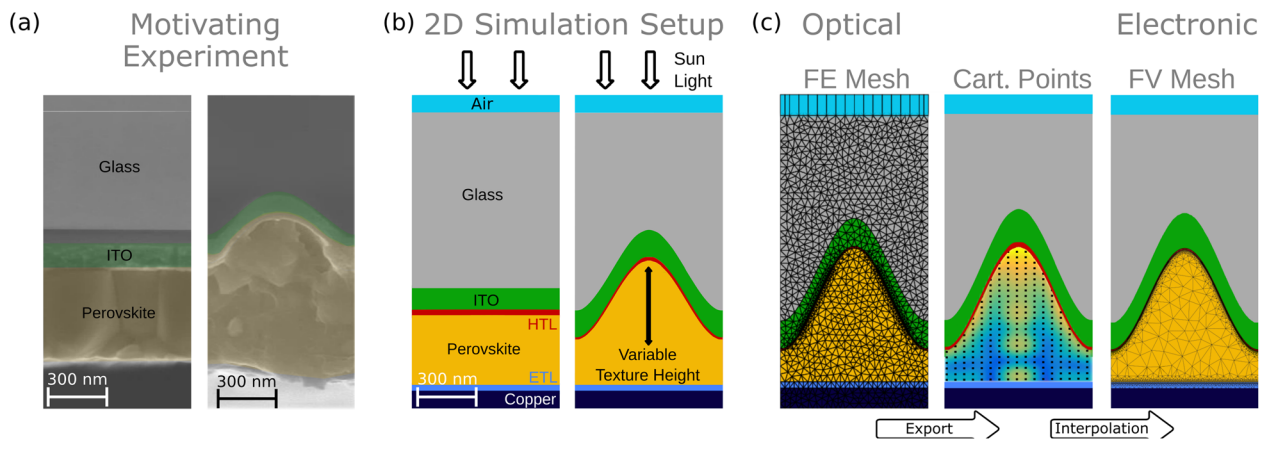

Fig. 1 Overview of motivating experimental devices, simulated stack and simulation methods used in this study. (a) Scanning electron microscope (SEM) cross-section micrograph of the physical layer stacks investigated by Tockhorn *et al.*[13] and Sutter,[15] showing planar (left) and textured (right) substrates. These devices showed improved efficiencies, which inspired the present work. The hole transport layer (HTL), electron transport layer (ETL), and the copper back contact layer are not visible. (b) The theoretical setup used for the optical and electronic simulations, depicting both planar (left) and textured (right) configurations. The material composition varies from the stacks in (a) and is taken from the literature[16–18] due to available electronic data from these sources. (c) Schematic illustration of the three-step coupling procedure between optical and electronic simulations: a finite element (FE) mesh for the optical simulation (left), Cartesian grid points used for exporting the photogeneration rate (middle), and a finite volume (FV) mesh for the electronic simulation (right).

been reported to show both increased and reduced open-circuit voltages for different devices.[9,13,14,19]

Fig. 1a shows cross-sectional scanning electron microscope (SEM) images of representative planar and sinusoidally textured substrates from previous studies.[13,15] Motivated by these experiments, our theoretical investigation is based on a well-characterised planar single-junction perovskite solar cell architecture,[16–18] for which detailed electronic data were reported. We extend this planar setup by incorporating two-dimensional (2D) sinusoidal nanotextures. The layer stack shown in Fig. 1b (left) consists of (from top to bottom) a glass substrate, an indium tin oxide (ITO) front electrode, a hole transport layer (HTL), a perovskite absorber (PVK), an electron transport layer (ETL), and a copper back contact. The absorber is a triple-cation perovskite with the composition $Cs_{0.05}(Fa_{83}MA_{17})_{0.95}PbI_{83}Br_{17}$. Moreover, PTAA is used as HTL, and C_{60} as ETL.

In the considered device, the dominant recombination pathways included in our model are radiative recombination,[36] non-radiative Shockley–Read–Hall recombination,[37,38] and interfacial recombination. Their mathematical formulations are provided in Section S2 of the SI. For many perovskite solar cells, interfacial recombination constitutes a major limitation to device performance.[16,39,40] In our specific configuration, Auger–Meitner recombination has only a minor influence on the power-conversion efficiency and is therefore neglected.[16]

We consider both planar and nanotextured versions of this architecture (Fig. 1b). The planar configuration (left) serves as a reference, while the nanotextured version (right) introduces sinusoidal textures at the glass/ITO, ITO/HTL, and HTL/PVK interfaces. Sinusoidal hexagonal nanotextures enabled a world-record power conversion efficiency for perovskite-silicon tandem solar cells between late 2021 and mid 2022.[20] Earlier work on single-junction perovskite solar cells showed that the optical and electronic performance of sinusoidal nanotextures was superior to that of inverted pyramids and pillars.[13] In those works, the perovskite layers were spin-coated, which is incompatible with state-of-the art pyramid textures that have been used for silicon solar cells for a long time.[41]

To reduce the computational load, we perform 2D simulations, assuming the textures to be invariant along the out-of-plane direction. The considered sinusoidal texture is given by

$$y(x) = h_T - h_T \cos\left(\frac{2\pi x}{w_T}\right), \quad (1)$$

where h_T is the variable texture height and $w_T = 750$ nm the period width, which is fixed for all texture heights.

We varied h_T between 0 nm (planar) and 750 nm. For the planar case, all layer thicknesses of the ETL (30 nm), PVK (400 nm), and HTL (10 nm) match the experimentally measured values.[17,18] For textured devices ($h_T > 0$ nm), we ensure that the total PVK volume remains constant across all configurations by adjusting the PVK thickness below the texture. This assumption guarantees that any increase in absorption is not due to an excess of material but only due to its distribution. As the texture height increases, the length of the PVK/HTL interface increases as well, while the ETL/PVK interface remains unchanged.

Finally, in Fig. 1c, we illustrate how the photogeneration data is transferred to the electronic charge transport simulations: first, the generation rate is computed on a finite element (FE) mesh (left panel) by solving the time-harmonic Maxwell equations. This data is then interpolated onto uniform Cartesian grid points for the data export (middle panel), and mapped onto a finite volume (FV) mesh (right panel) used in the drift-diffusion simulations. These simulations provide access to the total current density, spatial distributions of carrier concentrations, electric fields, and recombination rates.

As prototyping a series of different nanotextured cells is comparatively costly and does not readily yield physical insight into the electronic behaviour, we focus here on numerical simulations.

Influence of texturing on light absorption and carrier generation

Solar cells are driven by the power of the incident light with its characteristic spectrum. To compute the total reflectance, the absorptance in the different layers, and the photogeneration rate within the perovskite layer, we numerically solve the time-harmonic Maxwell equations in a scattering formulation.[33] The incident solar spectrum is discretised using monochromatic plane waves and weighted using the standardised AM1.5G reference spectrum.[42] We calculated the spectral absorption density $\mathscr{A}_{gen}(\lambda, \mathbf{x})$ for the relevant spectral range from $\lambda_1 = 300$ nm to $\lambda_2 = 900$ nm with 10 nm step size. The spectral absorption density quantifies where photons of a particular vacuum wavelength λ are absorbed, and integrating it over all wavelengths yields the photogeneration rate

$$G(\mathbf{x}) = \int_{\lambda_1}^{\lambda_2} \mathscr{A}_{gen}(\lambda, \mathbf{x}) \frac{\lambda}{hc} d\lambda, \quad (2)$$

which indicates where in the PVK layer the electron–hole pairs are generated. In the integral, the absorption density is divided by the photon energy $hc\lambda^{-1}$, where h is Planck's constant and c is the speed of light *in vacuo*. Fig. 2a shows the photogeneration rate G within the PVK layer for solar cells with no texture (left panel), an intermediate texture height of 300 nm (mid panel), and a large texture of 600 nm (right panel), all of which will be used in the electronic simulations in the next step. Integrating $\mathscr{A}_{gen}$ over the total perovskite area Ω_{PVK} gives the spectral absorptance

$$A_{gen}(\lambda) = \int_{\Omega_{PVK}} \mathscr{A}_{gen}(\lambda, \mathbf{x}) d\mathbf{x}. \quad (3)$$

Fig. 2b shows the spectral absorptance A_{gen} within the PVK layer (blue), the parasitic absorptance A_{par} in all remaining layers (red, purple, and pink) and reflectance R (grey), in the relevant spectral range, for the three device geometries discussed above. As known from previous work,[13,43] the texture reduces the total reflectance and thus leads to more absorption in the PVK layer increasing charge carrier generation. Further integrating either the absorptance over all wavelengths or the photogeneration rate over the area of the PVK layer Ω_{PVK}, one obtains the maximum achievable short-circuit current density

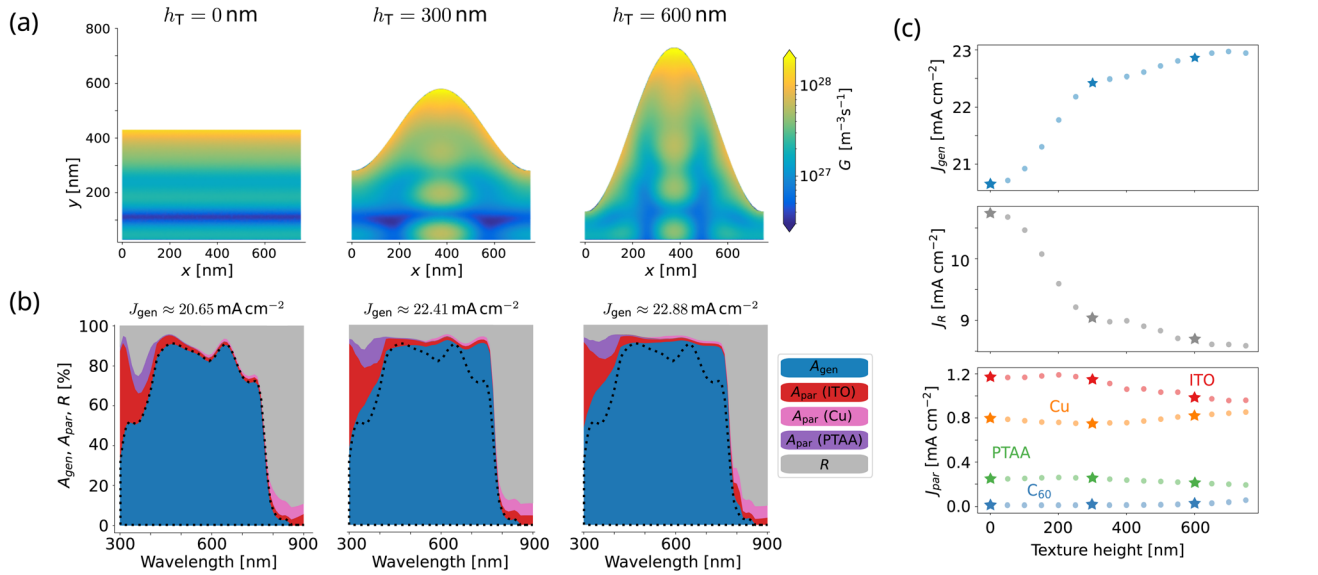

Fig. 2 (a) The optical photogeneration rate G plotted as a function of position in the perovskite layer for cells with no texture (left panel), 300 nm (mid panel), and 600 nm (right panel) nanotexture height. (b) Total spectral reflectance (R), parasitic absorptance (A_{par} in PTAA, Cu and ITO) and absorptance (A_{gen}) for no texture (left panel), 300 nm texture (mid panel), and 600 nm texture (right panel). The black dashed line indicates the absorptance for the non textured case of the first panel. The maximum achievable short-circuit current density J_{gen} calculated from the photogeneration rate within the perovskite absorber is stated above each panel, respectively. (c) Dependence of the maximum achievable short-circuit current density J_{gen} (top panel), the reflective losses J_R (mid panel), and the parasitic losses J_{par} (bottom panel) on texture height. The stars indicate the three textures shown in (a) and (b).

$$J_{gen} = \frac{q}{w_T}\int_{\lambda_1}^{\lambda_2} A_{gen}(\lambda)\frac{\lambda}{hc}\mathrm{d}\lambda = \frac{q}{w_T}\int_{\Omega_{PVK}} G(\mathbf{x})\mathrm{d}\mathbf{x}, \quad (4)$$

where q is the elementary charge and w_T is the texture width. The maximum achievable short-circuit current density J_{gen} serves as an upper bound to the short-circuit current density J_{SC}, since recombination prevents all generated electron–hole pairs from being collected at the contacts. How the texture height affects recombination losses is discussed later, for now it is enough to state that these losses are only small compared to gains in J_{gen}. Therefore, higher J_{gen} current densities lead directly to higher J_{SC} current densities. Fig. 2c (top panel) shows that J_{gen} strictly increases with texture height. Thus, J_{SC} gains are directly related to the improved optical properties of the textured devices.

To assess how much current density is lost *via* reflection and parasitic absorption, equivalent current densities J_R and J_i can be computed, where A_{gen} in (4) is replaced by $R(\lambda)$ or the parasitic absorption in the i-th layer. Fig. 2c (middle panel) shows the current density for the reflective losses J_R, which drops quickly with increasing texture height. Fig. 2c (right panel) shows J_{par} for the non-PVK layers of the device stack. Most notably, the losses in the ITO layer decrease slightly for higher textures. While the height of the ITO stays fixed, the texture increases the surface enhancement factor, effectively reducing its thickness for the incoming scattered light reducing the absorption in this layer. The same effect applies to the PTAA. Layers below the texture show a slight increase in their generated losses, due to an overall reduction in reflectance for all wavelengths.

Next, we export the results from the optical simulations to the electronic simulations by incorporating the photogeneration rates G (Fig. 2a) into the charge transport model. More precisely, this data serves as source term in the electron (α = n) and hole (α = p) drift-diffusion equations used in the electronic simulations,

$$z_\alpha q \partial_t n_\alpha + \nabla\cdot\mathbf{j}_\alpha = z_\alpha q[G(\mathbf{x}) - R(n_n, n_p)], \quad (5)$$

explained in more detail in Section S2 (SI). We simulate the charge transport of electrons and holes in the ETL, PVK layer and HTL for different texture heights (Fig. 3a, top) while also accounting for mobile ion vacancies in the PVK layer.

Behaviour of simulated PCE, J_{SC}, V_{OC}, and FF

In the following, we present simulation results, including current density–voltage (J–V) curves, open-circuit voltages V_{OC}, short-circuit current densities J_{SC}, power conversion efficiencies (PCEs), and fill factors (FFs).

The simulated J–V characteristics are obtained using a fast hysteresis measurement technique, designed to assess ionic redistribution losses at different scan speeds.[17] In this procedure, illustrated in Fig. 3a (bottom), the devices are held at a constant voltage near the open-circuit voltage ($V_{max} \geq V_{OC}$) for t_p seconds, followed by backward and forward voltage scans, each lasting $t_s = V_{max}/f$ seconds, where f denotes the scan rate.

All simulations use a fast scan rate of $f = 10^3$ V s^{-1}. At this rate, ionic motion is negligible, as shown in Fig. S5 and S10 (SI), where the vacancy density remains constant across different applied voltages. Throughout our study, the average vacancy concentration is fixed to 6.0×10^{22} m^{-3} within the perovskite layer,

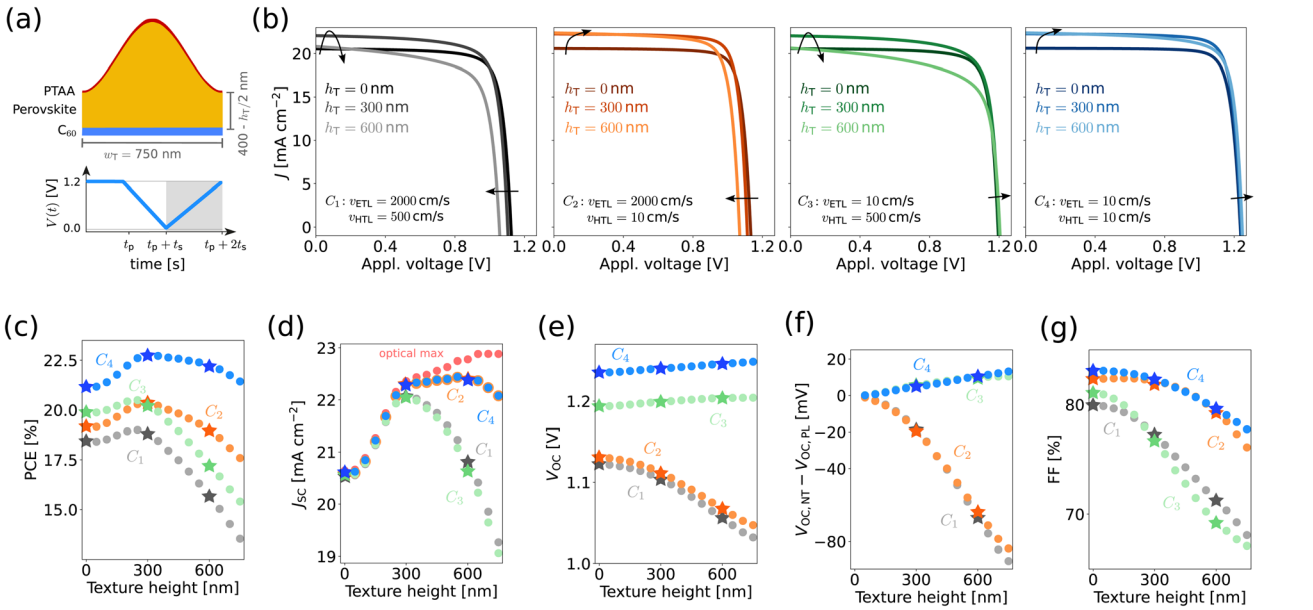

Fig. 3 Calculated performance metrics for the studied single-junction solar cell by solving the drift-diffusion charge transport model with a given optical photogeneration rate, computed from Maxwell's equations. (a) The device geometry (top) considered for the electronic simulations, consisting of the electron transport layer (C_{60}), the "83–17 triple cation" perovskite material layer, and the hole transport layer (PTAA). The thickness of the perovskite layer varies with the texture height h_T, while the texture width w_T stays the same. Moreover, the considered measurement protocol (bottom) includes a preconditioning step, a backward and a forward scan. The following simulation results correspond to the grey shaded forward scan. (b) Simulated forward current–voltage (J–V) curves for cases C_1 to C_4, where the surface recombination velocities v_{HTL} and v_{ETL} are varied. Brighter colours indicate greater texture height, with arrows showing the direction of increasing texture height. Furthermore, we show for all test cases C_1 (grey), C_2 (orange), C_3 (green), and C_4 (blue), the impact of texture height on (c) the power conversion efficiency (PCE), (d) the short-circuit current density J_{SC}, (e) the open-circuit voltage V_{OC}, (f) the difference in V_{OC} between planar (PL) and textured systems (NT), and (g) the fill factor (FF). The stars indicate the three texture heights shown in (b).

following values reported in the literature.[17] As ionic motion is suppressed at this scan rate, the device operates without hysteresis.[17,18] We therefore restrict our analysis to the forward scan.

Next, we extend the planar baseline to textured systems and investigate four scenarios with varying surface recombination velocities at the carrier transport layers. With increasing texture height, the PVK/HTL interface becomes longer, while the ETL/PVK interface remains unchanged. Case C_1 corresponds to the parameter set used by Thiesbrummel *et al.*[18] In the subsequent cases, we selectively reduce the surface recombination velocity at the HTL interface (C_2), at the ETL interface (C_3), or at both interfaces simultaneously (C_4). In other words, we have the test cases:

C_1: $v_{ETL} = 2000$ cm s^{-1}, $v_{HTL} = 500$ cm s^{-1} (ref. configuration 18).

C_2: $v_{ETL} = 2000$ cm s^{-1}, $v_{HTL} = 10$ cm s^{-1}.

C_3: $v_{ETL} = 10$ cm s^{-1}, $v_{HTL} = 500$ cm s^{-1}.

C_4: $v_{ETL} = 10$ cm s^{-1}, $v_{HTL} = 10$ cm s^{-1}.

Fig. 3b displays the J–V curves for cases C_1–C_4. Within each subfigure, brighter colours indicate larger texture heights, and arrows mark the direction of increasing texture height. In the reference case C_1, the short-circuit current density J_{SC} reaches its maximum at a texture height of $h_T = 300$ nm, but decreases again for larger values of h_T. The open-circuit voltage V_{OC}, however, decreases monotonically with texture height. Reducing the surface recombination velocity v_{HTL} at the HTL (C_2) has a beneficial effect on the J_{SC}: it increases consistently with texture height, while the behaviour of V_{OC} remains essentially unchanged compared with the reference case C_1. In contrast, reducing the surface recombination velocity at the ETL (C_3) leads to the opposite trend: the qualitative behaviour of J_{SC} (initial rise followed by a decline) is largely preserved, but V_{OC} now increases with texture height. When both surface recombination velocities are reduced (C_4), the advantages of both modifications (C_2) and (C_3) are combined, yielding an increase in both J_{SC} and V_{OC} for larger texture heights.

We analyse this behaviour quantitatively in the second row of Fig. 3c–g. We show the power conversion efficiency (PCE), the short-circuit current density J_{SC}, the open-circuit voltage V_{OC}, and the fill factor (FF) as functions of texture height for all test cases C_1 to C_4. All four configurations have maximal power conversion efficiencies (PCE, Fig. 3c) between $h_T = 250$ nm and $h_T = 300$ nm.

For all texture heights, the PCE of the reference case C_1 remains below that of the low-surface-recombination case C_4, while the mixed cases C_2 and C_3 yield PCE values between these two extremes. The origin of the PCE maximum near $h_T = 250$ nm or $h_T = 300$ nm can be attributed partly to the behaviour of the short-circuit current density J_{SC} (Fig. 3d), which deviates substantially from the maximum achievable short-circuit current density (red dots) beyond this texture height. The trends in J_{SC} with texture height for C_1 and C_3 (high v_{HTL}) behave similarly, as those do for C_2 and C_4 (low v_{HTL}), with the latter group staying much closer to the optical ideal.

Fig. 3e shows the dependence of the open-circuit voltage V_{OC} on texture height. Reducing v_{HTL} (C_2) has only a minor impact on V_{OC}, which continues to decrease with increasing texture height much like in the reference case (C_1). In contrast, reducing v_{ETL} significantly improves the open-circuit voltage (C_3 and C_4) and leads to an increasing V_{OC} with increasing texture height.

Although the sinusoidal texture increases the HTL interface area, changes in v_{HTL} (C_2) only weakly affect the V_{OC}. Instead, the dominant sensitivity arises from the *unchanged* ETL interface, where reducing v_{ETL} (C_3, C_4) markedly improves the V_{OC} and even reverses its trend with texture height. This behaviour indicates that ETL surface recombination mainly governs the device near open-circuit conditions, whereas the enlarged HTL interface has a stronger impact only at lower voltages. Interestingly, the absolute difference between the planar and textured open-circuit voltages behaves the same for C_1 and C_2 (high v_{ETL}), as well as for C_3 and C_4 (low v_{ETL}), as can be seen in Fig. 3f. Finally, the fill factor (FF) shown in Fig. 3g decreases with increasing texture height in all four cases.

Now let us put these results into perspective. Tockhorn *et al.*[13] reported results on a textured single-junction perovskite solar cell with 'cos-' texture of $h_T = 220$ nm texture height: for the forward scan, 0.6 $\%_{abs}$ absolute efficiency gain, 1 mA cm^{-2} increase in J_{SC}, 20 mV increase in V_{OC}, and 1 $\%_{abs}$ loss in the fill factor were observed with respect to a planar reference.

Our opto-electronic simulations exhibit similar trends to these experimental observations as summarised in Table 1. Specifically, for the reference configuration[18] C_1, the PCE is maximally increased by 0.6 $\%_{abs}$ for a texture height of 250 nm compared to a planar device. Significant increases greater than 1.0 $\%_{abs}$ in the PCE occur for the two test cases, where v_{HTL} (C_2 and C_4) is decreased. In all surface recombination velocity configurations the increase in J_{SC} is higher than 1.3 mA cm^{-2}. The losses in the fill factor behave roughly the same. In case of high v_{ETL} (C_1 and C_2), the losses in V_{OC} are >12 mV, while in case of low v_{ETL} (C_3 and C_4), the gains in V_{OC} are ≈4–5 mV.

The PCE is proportional to $J_{SC} \times V_{OC} \times FF$. For all test cases, the relative changes in J_{SC} are approximately an order of magnitude larger than those in V_{OC} and FF. Therefore, the enhancement in PCE arises primarily from the increases in short-circuit current density.

Table 1 Simulated current–voltage parameters for the planar system as well as for the textured systems with the highest power conversion efficiencies (PCEs). For the cases C_1 and C_3, the highest PCE is reached for $h_T = 250$ nm, while in the cases C_2 and C_4 for $h_T = 300$ nm

		PCE [%]	J_{SC} [mA cm^{-2}]	V_{OC} [V]	FF [%]
C_1	Planar	18.4	20.5	1.123	79.9
	Textured	19.0	21.9	1.110	78.1
C_2	Planar	19.2	20.6	1.131	82.4
	Textured	20.3	22.3	1.111	82.2
C_3	Planar	19.9	20.6	1.194	81.1
	Textured	20.5	21.9	1.198	78.0
C_4	Planar	21.2	20.6	1.235	83.1
	Textured	22.7	22.3	1.240	82.3

Finally, to estimate how much of the observed increase in V_{OC} can be attributed purely to the optical enhancement in J_{SC}, we use the classical Shockley diode relation for p–n junctions,[44] which gives

$$\Delta V_{OC} \approx \frac{k_B T}{q} \ln \delta_{SC}, \quad (6)$$

where $\delta_{SC} = J_{SC,NT}/J_{SC,PL}$ is the ratio of short-circuit current densities for the textured (NT) and planar (PL) systems, k_B is the Boltzmann constant, and T is the temperature. This expression assumes that the dark saturation current density J_0 is much smaller than J_{SC}, that J_0 remains constant for different texture heights, and that the ideality factor n is set to unity.

From Table 1, we find $\delta_{SC} \approx 1.07$ for C_3 and $\delta_{SC} \approx 1.08$ for C_4, yielding expected increases in V_{OC} of $\Delta V_{OC} \approx 1.75$ mV (C_3) and $\Delta V_{OC} \approx 2.01$ mV (C_4). By comparison, the simulated V_{OC} increase is roughly two to three times larger than this estimate, indicating that mechanisms, beyond the increase in J_{SC}, play a role.

In summary, our simulations show that reducing v_{HTL} keeps J_{SC} closer to the optical ideal as the texture height increases, which impacts the PCE the most. In contrast, lowering v_{ETL} can even counteract the detrimental impact of larger texture heights on V_{OC}. Across all configurations, the maximum PCE is attained near $h_T =$ 300 nm. To investigate the origin of these observations, we next examine the recombination processes in the simulated systems.

Impact of texturing on recombination currents

In this section, we identify the dominant recombination mechanisms across different voltage-bias regimes and analyse their influence on V_{OC}, J_{SC}, and consequently on the device efficiency. The individual recombination rates depend on the electron and hole densities, as detailed in the SI (Section S2). Throughout the forward scan, we first compute the carrier densities and subsequently evaluate the recombination rates in a post-processing step. For clarity, we restrict our discussion to the representative cases C_1 and C_4: (i) the reference configuration C_1, characterised by high surface recombination velocities v_{ETL} and v_{HTL}, and (ii) the low-surface-recombination configuration C_4, in which both v_{ETL} and v_{HTL} are strongly reduced. The intermediate cases C_2 and C_3 behave qualitatively like C_1 and C_4.

Fig. 4a displays the recombination current densities for planar devices in these two configurations for the forward scan. We show the radiative recombination current density J_{rad} (purple), the surface recombination current densities at the HTL interface $J_{SR,HTL}$ (blue) and at the ETL/PVK interface $J_{SR,ETL}$ (green), and the Shockley–Read–Hall (SRH) recombination current density J_{SRH} (red). For reference, the generation current density J_{gen} (yellow) is also included.

As expected from Thiesbrummel *et al.*,[18] the reference case C_1 exhibits dominant recombination at the ETL/PVK interface, as seen in Fig. 4a (left). In contrast, when both surface recombination velocities are strongly reduced (C_4), this suppression shifts the dominant loss mechanism to SRH recombination, as shown in Fig. 4a (right).

To analyse how nanotexturing alters these recombination rates, Fig. 4b–d show the texturing-induced changes in $J_{SR,HTL}$,

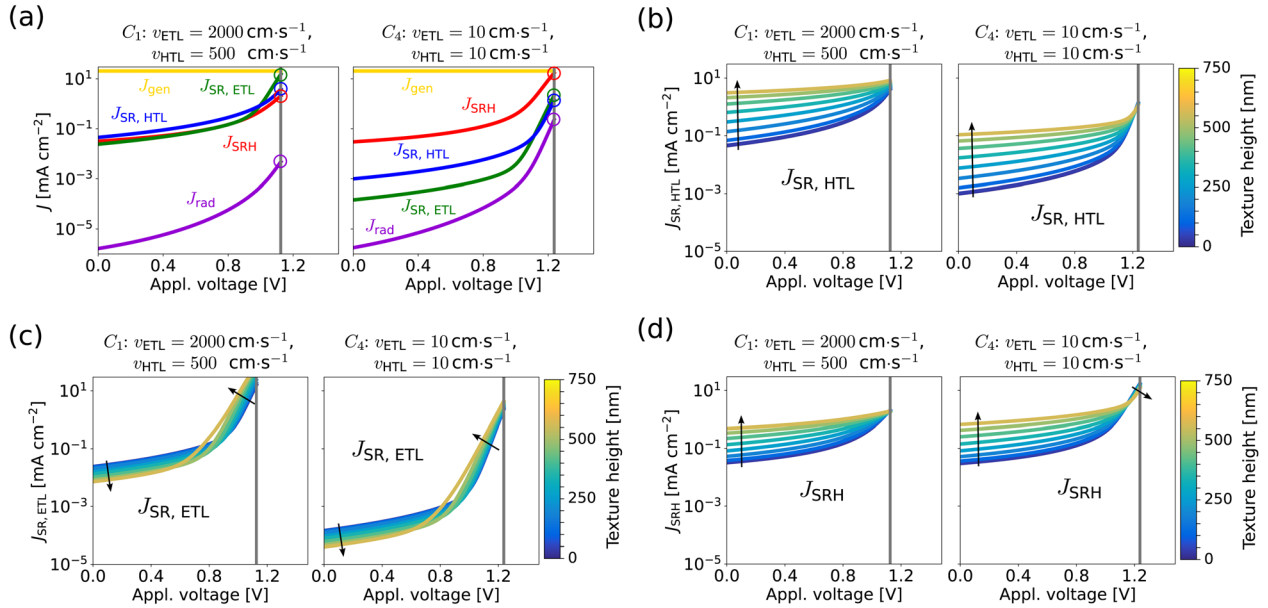

Fig. 4 Simulated voltage-dependent recombination current densities for planar and textured perovskite devices for the reference high-surface-recombination case C_1 (left) and the low-surface-recombination case C_4 (right) from drift-diffusion calculations, with the photogeneration rate obtained from Maxwell's equations. (a) Recombination current densities for the planar systems. We included radiative J_{rad} and surface recombination at the PVK/HTL $J_{SR,HTL}$ and ETL/PVK interfaces $J_{SR,ETL}$ as well as Shockley–Read–Hall (SRH) J_{SRH} recombination. These integrated recombination rates are compared to the generation current J_{gen}. Furthermore, we show for both recombination velocity test cases (b) $J_{SR,HTL}$, (c) $J_{SR,ETL}$, and (d) J_{SRH} for varying texture height. The grey vertical line indicates the open-circuit voltage of the planar configuration. The arrows indicate the direction of increasing texture height. Colour coding indicates device morphology: blue corresponds to planar devices and yellow to strongly textured devices.

$J_{SR,ETL}$, and J_{SRH}, respectively. The colour code spans from blue (planar device) to yellow (strong texture), and arrows indicate increasing texture height. Radiative recombination is orders of magnitude smaller than the other rates and largely unaffected by texturing, as shown in Fig. S1 (SI). Hence, it is not displayed here.

While the absolute magnitudes of the recombination currents shift depending on the chosen surface recombination velocities v_{HTL}, v_{ETL}, their qualitative dependence on texture height remains robust. For this reason, we focus on the following trends, where the first three trends are independent of the chosen surface recombination velocities:

(T1) J_{SC} conditions ($V = 0$ V): both $J_{SR,HTL}$ and J_{SRH} increase with texture height.

(T2) J_{SC} conditions ($V = 0$ V): $J_{SR,ETL}$ decreases with texture height.

(T3) Near V_{OC} conditions: $J_{SR,ETL}$ increases with texture height.

(T4) Near V_{OC} conditions (only for low v_{ETL}): J_{SRH} decreases with texture height.

The final trend (T4) is special because it appears only when the ETL surface recombination velocity is low, so that SRH recombination in the bulk becomes the dominant loss mechanism. In these bulk-recombination-dominated solar cells, the open-circuit voltage increases with texture height. Trend (T1) explains the strong impact of texturing on J_{SC} *via* increased HTL-side recombination, whereas a combination of (T3) and (T4) explains why texturing affects V_{OC} through increased ETL-side recombination.

For the intermediate cases C_2 and C_3, the recombination current densities $J_{SR,HTL}$ (Fig. S2), $J_{SR,ETL}$ (Fig. S3) and J_{SRH} (Fig. S4) are shown in the SI. These figures confirm that trends (T1) to (T3) also apply to these mixed cases. Trend (T4), however, appears only when v_{ETL} is sufficiently reduced for SRH recombination to become the dominant loss mechanism, as can be seen from Fig. S4 (SI).

These observations clarify the mechanisms behind the observed changes in J_{SC}, V_{OC}, and PCE: surface recombination at the HTL primarily affects J_{SC}, while recombination at the ETL mainly influences V_{OC}. The physical origin of trends (T1) to (T4) becomes apparent when examining the electric-field and carrier density configurations, which we analyse in the following subsection.

Effect of texturing on electric field and charge carriers

Fig. 5 shows the electric field and carrier densities of electrons and holes at different applied voltages for the low-surface-recombination case C_4 (low v_{ETL}, low v_{HTL}). For this velocity combination, all four previously discussed trends (T1)–(T4) are observed and can be explained.

Fig. 5a shows the electric field at short-circuit condition ($V = 0$ V). The electric field vectors, indicated by stream plots, point in the direction in which holes are driven by the field. Moreover, Fig. 5b visualizes the ratio between hole and electron density, while Fig. 5c shows one-dimensional cross sections of electron and hole densities near open-circuit voltage ($V = 1.2$ V).

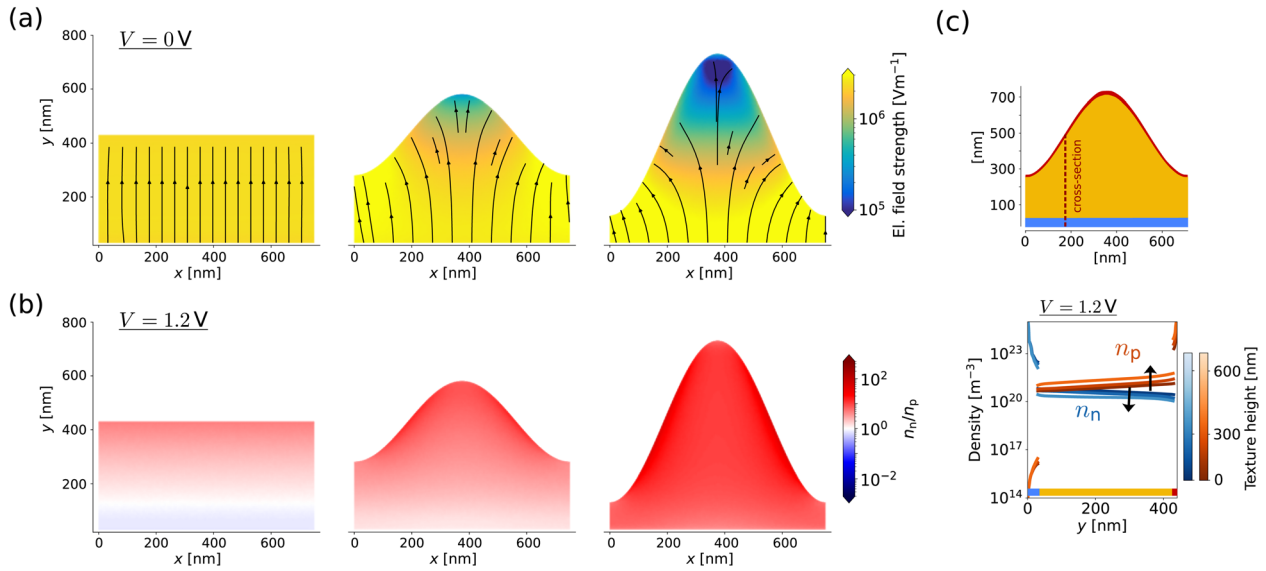

Fig. 5 (a) Electric field for three texture heights $h_T = 0$, 300, 600 nm for $V = 0$ V applied voltage. The colour and the stream plot indicate the strength $\|-\nabla\psi\|_2$ and the direction of the electric field, respectively. (b) The corresponding ratio between hole and electron density n_p/n_n for $V =$ 1.2 V applied voltage. (c) 2D device geometry with the vertical cross-section indicated (top), along which the carrier densities (bottom) are extracted. More precisely, we see one-dimensional profiles of the electron (blue) and hole densities (red) at an applied voltage $V = 1.2$ V for varying texture height. In the density plot, brighter colours indicate greater texture height, with arrows showing the direction of increasing texture height. All results correspond to the low-recombination case C_4.

At $V = 0$ V, the electric field is homogeneous in the planar configuration, but nanotexturing redistributes it: the field strengthens in the valleys and weakens at the peaks. Therefore, textured devices experience enhanced charge separation in the valleys, whereas the reduced field at the peaks leads to local carrier accumulation and thus increased recombination. This explains why HTL surface recombination and SRH recombination increase in trend (T1), whereas ETL surface recombination decreases at the beginning of the forward scan in trend (T2).

At higher applied voltages near open-circuit ($V = 1.2$ V), the internal electric field weakens and drift becomes negligible (SI, Fig. S8). We therefore analyse the carrier densities next, to understand the trends (T3) and (T4). From Fig. 5b, we find that the perovskite layer contains significantly more holes than electrons for textured systems as the device approaches open-circuit conditions. The inequality $n_p > n_n$ holds for all larger texture heights and across the entire perovskite layer. This results from the fact that increasing the texture height also increases the effective PVK/HTL interface length, increasing hole injection from the HTL. Consequently, more holes reach the ETL, and surface recombination at the ETL increases with texturing [trend (T3)].

Hou *et al.*[12] speculated that extended drift-dominated regions near the PVK/HTL interface were responsible for enhanced V_{OC} in textured perovskite solar cells. In contrast, we find that drift near the peaks is always reduced. Therefore, another mechanism must be responsible for the enhanced V_{OC} observed in nanotextured devices.

To understand trend (T4), the reduction of SRH recombination near open-circuit voltage, and by that the enhanced V_{OC} values, we examine Fig. 5c, which shows cross sections of the electron and hole densities. As shown in the SI (Fig. S7), the carrier densities vary minimally along the x-direction near $V \approx V_{OC}$. Therefore, in Fig. 5c we focus on one-dimensional cross-sections, which correspond to $x \approx 187$ nm, where the combined thickness of the ETL, perovskite (PVK) layer, and HTL is $y \approx 440$ nm for all texture heights.

A direct consequence of the rational form of the steady-state Shockley–Read–Hall expression is that the ratio n_p/n_n influences the recombination rate, even when the product $n_n n_p$ remains constant. For a deep defect, the SRH recombination rate is maximised for fixed $n_n n_p$, when $\tau_p n_n = \tau_n n_p$.[45] In our setup, the carrier lifetimes are equal.[16–18] Thus, SRH recombination is highest when $n_p/n_n \approx 1$. Fig. 5c (bottom) shows an increasing imbalance between electron and hole densities with increasing texture height. Specifically, we have $n_p > n_n$ (Fig. 5b), which directly decreases the SRH recombination rate for textured systems.

The quasi Fermi level splitting (QFLS), which is given by the energy difference between the electron and hole quasi Fermi levels, is a key quantity in determining the maximum achievable V_{OC}. The QFLS ΔE_F can be directly related to the product of electron and hole densities *via*

$$\Delta E_F = k_B T \ln\left(\frac{n_n n_p}{n_i^2}\right), \quad (7)$$

where n_i denotes the intrinsic carrier density.[44] It is well-established that in perovskite-based solar cells, the QFLS does not necessarily equal the open-circuit voltage V_{OC} when interfacial energy offsets are present.[39,46] The QFLS represents a theoretical upper limit for V_{OC}. In the ideal case of perfectly selective transport layers, we expect $\Delta E_F \approx qV_{OC}$. For a bias near open-circuit ($V = 1.2$ V), the integral average over the perovskite layer of the electron and hole densities $\overline{n_n n_p}$ increases with texture height (see SI, Fig. S7),

$$\sqrt{\overline{n_n n_p}} \approx 5.88 \times 10^{20}\ \mathrm{m}^{-3}, \quad \text{for } h_T = 0\ \mathrm{nm},$$
$$\sqrt{\overline{n_n n_p}} \approx 7.30 \times 10^{20}\ \mathrm{m}^{-3}, \quad \text{for } h_T = 600\ \mathrm{nm}.$$

Consequently, the logarithmic term in eqn (7) increases, lifting the upper limit for V_{OC} with increasing texture height.

Finally, the electric field and the carrier densities show the same qualitative behaviour for the reference surface recombination case C_1, as visualized in Fig. S9 (SI). The surface-recombination velocities modify only the magnitude of the resulting recombination rates, not the underlying qualitative trends (T1) to (T3) coming from texturing.

Conclusions

In this theoretical work, we build on the well-studied planar single-junction perovskite solar cell setup[16–18] to investigate how sinusoidal nanotextures between material layers affect device electronics. Multi-dimensional optical simulations were used to calculate the photogeneration rate, which served as input for subsequent electronic simulations. By analysing recombination rates, electric fields, and carrier distributions, we quantified how nanostructures influence the electronic performance of perovskite solar cells under different surface recombination configurations.

Texturing redistributes the electric field, strengthening it in valleys and weakening it at peaks, thereby affecting carrier accumulation and recombination dynamics. Across all recombination configurations, texturing improved the power conversion efficiency, with the highest values at a texture height of around 300 nm. Surface recombination plays a central role when texturing: the responses of J_{SC} and V_{OC} depend sensitively on the recombination velocities at the transport layers. Reducing the HTL recombination velocity helps to maintain the optical J_{SC} enhancement at larger texture heights, as texturing primarily increases HTL surface recombination at lower voltages. In contrast, lowering the ETL recombination velocity increases V_{OC} beyond what is expected from improved light absorption alone, because SRH recombination near V_{OC} conditions decreases with increasing texture height due to an increased carrier imbalance ($n_p > n_n$).

These findings provide clear design guidelines for high-efficiency nanotextured perovskite solar cells: effective passivation of the flat ETL interface is crucial to unlock V_{OC} gains, while passivation of the textured HTL interface is essential to maximize J_{SC} improvements. In addition, such topology optimization may lead to efficiency gains not only in solar cells but also in light-emitting diodes and photodetectors.

Methods

Optical model and simulation

For the optical simulations we numerically solve the time-harmonic wave equation as derived from Maxwell's equations, formulated as a scattering problem. We use the finite element method (FEM) as implemented in the software `JCMsuite`.[33] The computational domain consists of a unit cell comprising the layer stack shown in Fig. 1b. We use periodic boundary conditions in the x-direction and assume the top and bottom (y-direction) to be filled with infinite half-spaces of glass and air, respectively, which is numerically treated with perfectly matched layers (PMLs) as transparent boundary conditions. For the z-direction we assume translational invariance of the geometry. In a real solar cell, the glass has a finite thickness in the order of millimetres, which cannot be efficiently handled by full-field simulations. To account for the air-glass interface on top of the solar cell, we correct for the initial reflection at this interface, which is around 4% for normal incidence. For the 2D simulations, the solar cell stack is discretised with an unstructured, triangular mesh with element side lengths between 3 nm and 50 nm, and we use polynomials of degree 3 to approximate the solution within each element. The solar spectrum is sampled in the range of $\lambda_1 = 300$ nm to $\lambda_2 = 900$ nm with 10 nm step size. The incident light is modelled as a plane wave incident from the top, *i.e.*, propagating from $+y$ to $-y$. The used material properties are specified in the SI in Section S1(B). They consist of tabulated n, k values obtained from various sources. The simulation yields the local absorption density $\mathscr{A}_{gen}$ which is numerically integrated according to eqn (2) and (3) to obtain the photogeneration rate $G(\mathbf{x})$ and the absorptance A_{gen}. Likewise the current densities J_{gen}, J_{par} and J_R are obtained by numerically integrating A_{gen}, A_{par} and R according to (4). The numerical settings for the optical simulations are chosen such that a relative numerical accuracy of better than 10^{-3} is obtained for the exported photogeneration profile and the calculated maximal achievable current density J_{gen}. Section S4 of the SI contains a convergence scan for both of these outputs.

Electronic model and simulation

We employ a vacancy-assisted drift-diffusion model for the electronic simulations to describe the charge transport in the solar cells which is detailed in the SI. The movement of electrons and holes is considered in the ETL, PVK layer, and HTL. Within the perovskite layer, the dynamics of ionic vacancies are also taken into account.[35,47] Charge carrier motion is governed by drift-diffusion equations, which are self-consistently coupled to the Poisson equation *via* the electrostatic potential.[48] These equations are solved using a time-implicit finite volume scheme[49] with the excess chemical potential flux scheme for the current density approximation,[50] implemented in `ChargeTransport.jl`,[34] which builds on the finite volume solver `VoronoiFVM.jl`.[51] The finite volume method has the major advantage of correctly reflecting physical phenomena such as local conservativity of fluxes and consistency with thermodynamic laws.[48,52] For the time discretization, we rely on an implicit Euler method. The resulting non-linear system is solved using a damped Newton method, with the associated linear systems solved *via* the sparse direct solver `UMFPACK`.[53] We generate a boundary conforming Delaunay triangulation of the computational domain using `Triangle`,[54] which allows to define the dual Voronoi mesh, providing the control volumes for the finite volume method. Particular attention is paid to accurately resolving the internal material interfaces, as shown in Fig. 1c (right). The spatial mesh contains between 47 122 nodes (planar) and 143 713 nodes (textured with $h_T = 750$ nm). The temporal mesh for the voltage scan protocol is build adaptively: the time step size is dynamically adjusted based on convergence

behaviour, with minimum and maximum step sizes of $\Delta t_{min} = 6.0 \times 10^{-8}$ s and $\Delta t_{max} = 8.0 \times 10^{-8}$ s (for fast scans), resulting in approximately 150 time steps for the forward scan.

Combining the optical and electronic model

As illustrated in Fig. 1c (left), the simulation workflow begins with `JCMsuite`, which solves the time-harmonic Maxwell equations and computes the optical photogeneration rate in a post-processing step. This rate is then interpolated onto a uniform 300 × 1000 Cartesian grid (Fig. 1c, middle) and used as input for the electronic simulations performed with `ChargeTransport.jl` (Fig. 1c, right). Specifically, the photogeneration rate acts as a source term in the electron and hole continuity equations. For this purpose, the optical input data is linearly interpolated *via* `Interpolations.jl`[55] and then further mapped onto the finite volume nodes. Details of both models, along with all physically relevant material parameters, are provided in the SI. The simulation codes to reproduce the opto-electronic results are available in the associated data publication linked to this manuscript.[56]

Author contributions

D. A. prepared, performed and analysed the opto-electronic simulations. J. R. prepared, performed and analysed the optical simulations. D. A., P. F., J. F., and P. J. prepared the data publication. P. J. gave advice on the opto-electronic software. T. K. gave advice on the discussion of the open-circuit voltage enhancement. C. B., S. B., and K. J. supervised the optical simulations. P. F. and J. F. supervised the opto-electronic simulations. D. A. and P. F. coordinated the project. D. A., C. B., P. F., K. J., and J. R. wrote the initial manuscript, and all authors participated in proofreading and correcting the manuscript. C. B., S. B., P. F., and K. J. initiated the project.

Conflicts of interest

The authors declare no conflicts of interest.

Data availability

Alongside our manuscript, we provide a data repository.[56] This repository transparently and reproducibly documents all simulations performed with the software package `ChargeTransport.jl`[34] for generating the opto-electronic results. It includes all scripts and data files necessary to reproduce the opto-electronic figures.

Supplementary information (SI): optical and electronic simulation models and material parameters used in this work, additional electronic results including recombination currents and carrier distributions, and an optical convergence study of the photogeneration profile and the corresponding maximal short-circuit current density. See DOI: https://doi.org/10.1039/d5el00208g.

Acknowledgements

This project was supported by the Leibniz competition 2020 (NUMSEMIC, J89/2019) as well as the Deutsche Forschungsgemeinschaft (DFG, German Research Foundation) under Germany's Excellence Strategy – The Berlin Mathematics Research Center MATH+ (EXC-2046/1, project ID: 390685689). It also has received funding from the German Federal Ministry of Education and Research (BMBF Forschungscampus MODAL, project number 05M20ZBM). We thank Johannes Sutter for providing the SEM images of the studied layer stacks, which were taken during his time at HZB. Further, we thank Martin Hammerschmidt, Lin Zschiedrich, and Phillip Manley from JCMwave GmbH for fruitful discussions and support. The optical simulations were obtained in the framework of the Berlin Joint Lab for Optical Simulations for Energy Research (BerOSE) of Helmholtz-Zentrum Berlin für Materialien und Energie, Zuse-Institut Berlin, and Freie Universität Berlin.

Notes and references

1 J. Han, K. Park, S. Tan, Y. Vaynzof, J. Xue, E. W.-G. Diau, M. G. Bawendi, J.-W. Lee and I. Jeon, *Nat. Rev. Methods Primers*, 2025, **5**, 3.
2 A. S. R. Bati, Y. L. Zhong, P. L. Burn, M. K. Nazeeruddin, P. E. Shaw and M. Batmunkh, *Commun. Mater.*, 2023, **4**, 2.
3 K. Jäger, U. Aeberhard, E. Alarcon Llado, B. Bläsi, S. Burger, B. Ehrler, W. Favre, A. Fejfar, T. Gageot, I. Gordon, H. Helmers, O. Höhn, O. Isabella, M. Jošt, M. Ledinský, J. Mandal, P. Manley, D. Muñoz, Z. Omair, J. C. Ortiz Lizcano, U. W. Paetzold, A. P. Raman, H. Sai, R. Saive, M. Schmid, E. Yablonovitch and C. Becker, *Adv. Opt. Photonics*, 2025, **17**, 185–294.
4 Y. Wang, R. Lin, C. Liu, X. Wang, C. Chosy, Y. Haruta, A. D. Bui, M. Li, H. Sun, X. Zheng, H. Luo, P. Wu, H. Gao, W. Sun, Y. Nie, H. Zhu, K. Zhou, H. T. Nguyen, X. Luo, L. Li, C. Xiao, M. I. Saidaminov, S. D. Stranks, L. Zhang and H. Tan, *Nature*, 2024, **635**, 867–873.
5 J. Liu, Y. He, L. Ding, H. Zhang, Q. Li, L. Jia, J. Yu, T. W. Lau, M. Li, Y. Qin, X. Gu, F. Zhang, Q. Li, Y. Yang, S. Zhao, X. Wu, J. Liu, T. Liu, Y. Gao, Y. Wang, X. Dong, H. Chen, P. Li, T. Zhou, M. Yang, X. Ru, F. Peng, S. Yin, M. Qu, D. Zhao, Z. Zhao, M. Li, P. Guo, H. Yan, C. Xiao, P. Xiao, J. Yin, X. Zhang, Z. Li, B. He and X. Xu, *Nature*, 2024, **635**, 596–603.
6 Z. Liu, R. Lin, M. Wei, M. Yin, P. Wu, M. Li, L. Li, Y. Wang, G. Chen, V. Carnevali, L. Agosta, V. Slama, N. Lempesis, Z. Wang, M. Wang, Y. Deng, H. Luo, H. Gao, S. M. Rothlisberger, U. Zakeeruddin, X. Luo, Y. Liu, M. Grätzel and H. Tan, *Nat. Mater.*, 2025, **24**, 252–259.
7 L. Wang, N. Wang, X. Wu, B. Liu, Q. Liu, B. Li, D. Zhang, N. Kalasariya, Y. Zhang, X. Yan, J. Wang, P. Zheng, J. Yang, H. Jin, C. Wang, L. Qian, B. Yang, Y. Wang, X. Cheng, T. Song, M. Stolterfoht, X. C. Zeng, X. Zhang, M. Xu, Y. Bai, F. Xu, C. Zhou and Z. Zhu, *Adv. Mater.*, 2025, **37**, 2416150.
8 E. Ugur, A. A. Said, P. Dally, S. Zhang, C. E. Petoukhoff, D. Rosas-Villalva, S. Zhumagali, B. K. Yildirim, A. Razzaq, S. Sarwade, *et al.*, *Science*, 2024, **385**, 533–538.
9 U. W. Paetzold, W. Qiu, F. Finger, J. Poortmans and D. Cheyns, *Appl. Phys. Lett.*, 2015, **106**, 173101.
10 F. Sahli, J. Werner, B. A. Kamino, M. Bräuninger, R. Monnard, B. Paviet-Salomon, L. Barraud, L. Ding,

J. J. Diaz Leon, D. Sacchetto, G. Cattaneo, M. Despeisse, M. Boccard, S. Nicolay, Q. Jeangros, B. Niesen and C. Ballif, *Nat. Mater.*, 2018, **17**, 820–826.

11 B. Chen, Z. J. Yu, S. Manzoor, S. Wang, W. Weigand, Z. Yu, G. Yang, Z. Ni, X. Dai, Z. C. Holman and J. Huang, *Joule*, 2020, **4**, 850–864.

12 Y. Hou, E. Aydin, M. De Bastiani, C. Xiao, F. H. Isikgor, D.-J. Xue, B. Chen, H. Chen, B. Bahrami, A. H. Chowdhury, A. Johnston, S.-W. Baek, Z. Huang, M. Wei, Y. Dong, J. Troughton, R. Jalmood, A. J. Mirabelli, T. G. Allen, E. Van Kerschaver, M. I. Saidaminov, D. Baran, Q. Qiao, K. Zhu, S. De Wolf and E. H. Sargent, *Science*, 2020, **367**, 1135–1140.

13 P. Tockhorn, J. Sutter, R. Colom, L. Kegelmann, A. Al-Ashouri, M. Roß, K. Jäger, T. Unold, S. Burger, S. Albrecht and C. Becker, *ACS Photonics*, 2020, **7**, 2589–2600.

14 H. Winarto, J. Sutter, P. Tockhorn, V. Škorjanc, P. Patil, S. Berwig, L. Zimmermann, G. Martínez-Denegri, S. Albrecht and C. Becker, *Sol. RRL*, 2025, e202500613.

15 J. Sutter, PhD thesis, Technische Universität Berlin, 2022.

16 J. Diekmann, P. Caprioglio, M. H. Futscher, V. M. Le Corre, S. Reichert, F. Jaiser, M. Arvind, L. P. Toro, E. Gutierrez-Partida, F. Peña Camargo, C. Deibel, B. Ehrler, T. Unold, T. Kirchartz, D. Neher and M. Stolterfoht, *Sol. RRL*, 2021, **5**, 2100219.

17 V. M. Le Corre, J. Diekmann, F. Peña-Camargo, J. Thiesbrummel, N. Tokmoldin, E. Gutierrez-Partida, K. P. Peters, L. Perdigón-Toro, M. H. Futscher, F. Lang, J. Warby, H. J. Snaith, D. Neher and M. Stolterfoht, *Sol. RRL*, 2022, **6**, 2100772.

18 J. Thiesbrummel, S. Shah, E. Gutierrez-Partida, F. Zu, F. Peña-Camargo, S. Zeiske, J. Diekmann, F. Ye, K. P. Peters, K. O. Brinkmann, P. Caprioglio, A. Dasgupta, S. Seo, F. A. Adeleye, J. Warby, Q. Jeangros, F. Lang, S. Zhang, S. Albrecht, T. Riedl, A. Armin, D. Neher, N. Koch, Y. Wu, V. M. Le Corre, H. Snaith and M. Stolterfoht, *Nat. Energy*, 2024, **9**, 664–676.

19 J. Liu, M. De Bastiani, E. Aydin, G. T. Harrison, Y. Gao, R. R. Pradhan, M. K. Eswaran, M. Mandal, W. Yan, A. Seitkhan, *et al.*, *Science*, 2022, **377**, 302–306.

20 P. Tockhorn, J. Sutter, A. Cruz, P. Wagner, K. Jäger, D. Yoo, F. Lang, M. Grischek, B. Li, J. Li, O. Shargaieva, E. Unger, A. Al-Ashouri, E. Köhnen, M. Stolterfoht, D. Neher, R. Schlatmann, B. Rech, B. Stannowski, S. Albrecht and C. Becker, *Nat. Nanotechnol.*, 2022, **17**, 1214–1221.

21 J. Zheng, H. Wei, Z. Ying, X. Yang, J. Sheng, Z. Yang, Y. Zeng and J. Ye, *Adv. Energy Mater.*, 2023, **13**, 2203006.

22 O. Er-Raji, C. Messmer, A. J. Bett, O. Fischer, S. K. Reichmuth, F. Schindler, M. Bivour, O. Schultz-Wittmann, J. Borchert, M. Hermle, *et al.*, *Sol. RRL*, 2023, **7**, 2300659.

23 C. M. Wolff, P. Caprioglio, M. Stolterfoht and D. Neher, *Adv. Mater.*, 2019, **31**, 1902762.

24 M. T. Neukom, A. Schiller, S. Züfle, E. Knapp, J. Ávila, D. Pérez-del Rey, C. Dreessen, K. P. Zanoni, M. Sessolo, H. J. Bolink and B. Ruhstaller, *ACS Appl. Mater. Interfaces*, 2019, **11**, 23320–23328.

25 U. Aeberhard, S. J. Zeder and B. Ruhstaller, *Sol. RRL*, 2024, **8**, 2400264.

26 C. Messmer, D. Chojniak, A. J. Bett, S. K. Reichmuth, J. Hohl-Ebinger, M. Bivour, M. Hermle, J. Schön, M. C. Schubert and S. W. Glunz, *Prog. Photovoltaics*, 2025, **33**, 126–142.

27 W. Clarke, L. Bennett, Y. Grudeva, J. Foster, G. Richardson and N. Courtier, *J. Comput. Electron.*, 2022, **22**, 364–382.

28 P. Calado, I. Gelmetti, B. Hilton, M. Azzouzi, J. Nelson and P. R. F. Barnes, *J. Comput. Electron.*, 2022, **21**, 960–991.

29 M. Koopmans, V. M. Le Corre and L. J. A. Koster, *J. Open Source Softw.*, 2022, **7**, 3727.

30 S. Tahir, S. Mushtaq, J. McQueen, J. Iqbal, R. S. Almufarij, R. S. Alqurashi, R. S. Bonilla and A. Ashfaq, *Sci. Rep.*, 2025, **15**, 20020.

31 C.-H. Hsieh, J.-Y. Huang and Y.-R. Wu, *J. Appl. Phys.*, 2024, **135**, 115002.

32 J.-Y. Huang, E.-W. Chang and Y.-R. Wu, *IEEE J. Photovolt.*, 2019, **9**, 1686–1692.

33 J. Pomplun, S. Burger, L. Zschiedrich and F. Schmidt, *Phys. Status Solidi B*, 2007, **244**, 3419.

34 D. Abdel, P. Farrell, J. Fuhrmann and P. Jaap, *ChargeTransport.jl – Simulating Charge Transport in Semiconductors*, 2024, DOI: 10.5281/zenodo.13897997.

35 D. Abdel, P. Vágner, J. Fuhrmann and P. Farrell, *Electrochim. Acta*, 2021, **390**, 138696.

36 W. van Roosbroeck and W. Shockley, *Phys. Rev.*, 1954, **94**, 1558–1560.

37 W. Shockley and W. T. Read, *Phys. Rev.*, 1952, **87**, 835–842.

38 R. N. Hall, *Phys. Rev.*, 1952, **87**, 387.

39 M. Stolterfoht, P. Caprioglio, C. M. Wolff, J. A. Márquez, J. Nordmann, S. Zhang, D. Rothhardt, U. Hörmann, Y. Amir, A. Redinger, L. Kegelmann, F. Zu, S. Albrecht, N. Koch, T. Kirchartz, M. Saliba, T. Unold and D. Neher, *Energy Environ. Sci.*, 2019, **12**, 2778–2788.

40 C. M. Wolff, F. Zu, A. Paulke, L. P. Toro, N. Koch and D. Neher, *Adv. Mater.*, 2017, **29**, 1700159.

41 J. Haynos, J. Allison, R. Arndt and A. Meulenberg, *Int. Conf. on Photovoltaic Power Generation*, Hamburg, Germany, 1974, p. 487.

42 U.S. Department of Energy (DOE)/NREL/ALLIANCE, *Reference Air Mass 1.5 Spectra*, https://www.nrel.gov/grid/solar-resource/spectra-am1.5.html, accessed on 5 Jan 2026.

43 D. Chen, P. Manley, P. Tockhorn, D. Eisenhauer, G. Köppel, M. Hammerschmidt, S. Burger, S. Albrecht, C. Becker and K. Jäger, *J. Photonics Energy*, 2018, **8**, 022601.

44 P. Würfel and U. Würfel, *Physics of Solar Cells: from Basic Principles to Advanced Concepts*, Wiley-VCH Verlag GmbH & Co, Weinheim, 3rd edn, 2016.

45 J. Hüpkes, U. Rau and T. Kirchartz, *Sol. RRL*, 2022, **6**, 2100720.

46 P. Caprioglio, M. Stolterfoht, C. M. Wolff, T. Unold, B. Rech, S. Albrecht and D. Neher, *Adv. Energy Mater.*, 2019, **9**, 1901631.

47 D. Abdel, PhD thesis, Freie Universität Berlin, 2024.

48 P. Farrell, D. H. Doan, M. Kantner, J. Fuhrmann, T. Koprucki and N. Rotundo, *Handbook of Optoelectronic Device Modeling and Simulation: Lasers, Modulators, Photodetectors, Solar Cells, and Numerical Methods*, CRC Press Taylor & Francis Group, 2017, vol. 2, pp. 733–771.

49 D. Abdel, C. Chainais-Hillairet, P. Farrell and M. Herda, *IMA J. Numer. Anal.*, 2024, **44**, 1090.
50 D. Abdel, P. Farrell and J. Fuhrmann, *Opt. Quantum Electron.*, 2021, **53**, 163.
51 J. Fuhrmann, P. Jaap, D. Runge, D. Abdel, J. Weidner, A. Seiler, P. Farrell and M. Liero, *VoronoiFVM.jl - Finite volume solver for coupled nonlinear partial differential equations*, 2025, DOI: 10.5281/zenodo.15161153.
52 C. Chainais-Hillairet and M. Herda, *IMA J. Numer. Anal.*, 2019, **40**, 2473–2504.
53 T. A. Davis, *ACM Trans. Math. Softw.*, 2004, **30**, 196–199.
54 J. R. Shewchuk, *Applied Computational Geometry towards Geometric Engineering*, 1996, pp. 203–222.
55 M. Kittisopikul, T. E. Holy and T. Aschan, *Interpolations.jl*, 2025, https://github.com/JuliaMath/Interpolations.jl.
56 D. Abdel, J. Relle, T. Kirchartz, P. Jaap, J. Fuhrmann, S. Burger, C. Becker, K. Jäger and P. Farrell, *TexturedPerovskiteSolarCells.jl – Numerical examples to analyse the electronic behaviour of textured perovskite solar cells*, 2025, https://github.com/NUMSEMIC/TexturedPerovskiteSolarCells.jl.